# Dynamic control of the permanent magnet-assisted reluctance synchronous machine

H.W. de Kock and M.J. Kamper

**Abstract:** A digital signal processor-based control system for the permanent magnet-assisted reluctance synchronous machine, with the emphasis on dynamic performance, is proposed. A classical design approach is used to design the current and speed controllers for the machine. The stator current of the machine is controlled in such a way that the current angle in the *dq* synchronous reference frame is constant. The load–torque is estimated using a state space observer and compensation current based on the estimated load is used to improve the dynamic performance of the drive. The control system design is machine specific as it relies on data from finite-element analysis. Simulated and measured results on a 110-kW power level show that the resulting control system is stable and robust with good dynamic performance.

## 1 Introduction

The permanent magnet-assisted reluctance synchronous machine (PMA-RSM) is an interior PM synchronous machine (IPM-SM), however, the greatest torque producing component is the reluctance torque due to the large rotor saliency. The IPM-SM, RSM and PMA-RSM share many properties, but essentially the PMA-RSM is a well-designed RSM with additional minimised PM. It has been shown that the rotor designs with large saliency and minimised PM is the best choice for flux-weakening performance [1]. The PMA-RSM exhibits a good constant-power speed range and is ideal for traction applications such as electrical vehicles [2].

Machines with large rotor saliency exhibit peculiar features due to their particular flux–current relationship [3]. Moreover, precise speed control of such drives becomes a complex issue owing to the nonlinear speed–voltage coupling terms in the voltage equations as well as the nonlinearity present in the torque equation [4]. In this regard, several approaches to the control problem have been suggested [1, 3–14].

For synchronous machines, it is common to quantify control variables such as flux linkage, voltage and current with respect to a *dq* reference frame that is synchronous with the rotor. In most cases, torque control is achieved indirectly by controlling the $i_d$, $i_q$ components of the current vector $\boldsymbol{i}_s$ [4–12], whereas in some cases, the flux linkage $\lambda_d$ and current $i_q$ combination is chosen as control variables [1, 3]. In another approach, the torque is controlled directly [13, 14].

In the case where $i_d$ and $i_q$ are used as control variables, Betz *et al.* [7] show that there is set of control strategies namely (1) maximum torque per ampere control, (2) maximum rate of change of torque control, (3) maximum power factor control and (4) constant field current control. Although in some cases constant field current control is used [11], it is generally agreed that energy efficiency is very important and therefore maximum torque per ampere control is widely used [5, 6, 8–10].

There are different methods to obtain maximum torque per ampere control. Many of these methods use extensive mathematical derivations. In contrast, the use of finite-element (FE) analysis to determine the optimal control strategy for the machine is rather simple and it has the advantage of taking the effects of saturation and cross-magnetisation into account [8]. It has been shown that the maximum torque per ampere locus on the *dq* current plane, for the constant-torque speed region, can be approximated by a constant current angle locus [8]. Therefore the use of constant current angle control (CCAC) for speeds below base speed, results in close to optimal efficiency for all load conditions.

Machine design using FE computer programs is widely accepted, especially when nonlinear magnetic behaviour plays a key role [15, 16]. FE software with built in optimisation algorithms can be used to design electrical machines that give optimal performance [16, 17]. The control system coupled to the machine plays an equally important role, though, because it needs to control the machine at the optimal operating points. The availability and popularity of FE software together with the processing power of modern digital control hardware has lent itself to the inclusion of FE analysis results, in the form of lookup tables (LUTs), in the control algorithm [1, 5]. This machine specific type of algorithm results in a robust control system with optimal performance, but it requires the results from FE analysis.

This paper focuses on the dynamic control of the PMA-RSM in the constant-torque speed region. FE analysis results are used extensively to obtain an energy efficient, stable and robust control system with good dynamic performance. A classical design approach is used to design the current and speed controllers and CCAC is employed. The dynamic performance is then improved by estimating the load–torque and calculating a correct compensation current, which is added to the current reference. This paper shows that a well-known design



doi:10.1049/iet-epa:20060325

Paper first received 23rd August and in revised form 19th November 2006

The authors are with the Electrical Machines Laboratory, Department of Electrical Engineering, University of Stellenbosch, Private Bag X1, Matieland 7602, South Africa

E-mail: hugo@sun.ac.za

approach can be greatly improved using results from FE analysis.

## 2 Background and mathematical model

The rotor of a 110 kW RSM was designed using FE software with incorporated optimisation algorithms [16]. A small amount of PM was then added to the rotor to improve the performance in the flux weakening region [17]. Fig. 1*a* shows a cross-section of the optimally designed reluctance rotor with the PM material inside the flux barriers. Fig. 1*b* is a vector diagram that defines the current and flux linkage vectors with their respective angles and *dq* components.

FE analysis results of the generated torque as a function of the current angle $\phi$, for different current magnitudes, that is different load conditions of the PMA-RSM, are shown in Fig. 2*a*. In this graph, the filled circles indicate the maximum torque per ampere points; it shows that the most appropriate current angle for positive torque is between $45^\circ < \phi < 60^\circ$, and for negative torque between $120^\circ < \phi < 135^\circ$. If the current angle corresponding to the maximum torque at rated current is chosen as a constant current angle reference $\phi^*$ for all load conditions, the loss in torque (or efficiency) is very small at non-rated load conditions; it is therefore a reasonable approximation. For this case, $\phi^* = 54^\circ$ is chosen for positive torque and $\phi^* = 126^\circ$ for negative torque, as shown in Table 1.

The polar graph in Fig. 2*b* shows the absolute value of the machine's torque (modulus) as a function of current angle (argument), at rated current magnitude. The sign of the torque is indicated in each quadrant. The polar representation makes it clear that the current of the PMA-RSM should be controlled in the upper half of the current plane, so that the machine has equal motoring and generating capabilities. An important conclusion is therefore that constant field current control cannot be used for the PMA-RSM. The torque equation in terms of the current vector $\boldsymbol{i}_s = i_s\angle\phi$ for the PMA-RSM is given by

$$\begin{aligned} T_{\text{em}} &= \frac{3}{2}p[\lambda_d \cdot i_q - (\lambda_{qi} + \lambda_{\text{pm}}) \cdot i_d] \\ &= \frac{3}{2}p(\lambda_d \cdot i_q - \lambda_q \cdot i_d) \\ &= \frac{3}{2}p(\lambda_d \sin\phi - \lambda_q \cos\phi) \cdot i_s \end{aligned} \tag{1}$$

In (1), $T_{\text{em}}$ is the torque produced due to the interaction of the current components $i_d, i_q$ and the flux linkage components $\lambda_d, \lambda_{qi}, \lambda_{\text{pm}}$, where $\lambda_{qi}$ is due to $i_q$ and $\lambda_{\text{pm}}$ due to the PMs. Superposition of $\lambda_{qi}$ and $\lambda_{\text{pm}}$ is justified, as the flux barriers allow little saturation in the $q$-axis direction. The number of pole pairs is denoted by $p$. Equation (1) connects the mechanical model of the machine-system, given by (2), to the electrical model of the machine, given by (3) and (4). The relationship between the electrical speed and the mechanical speed of the machine is given by (5)

$$T_{\text{em}} = T_{\text{L}} + J_{\text{eq}}\frac{d\omega_m}{dt} + B_{\text{eq}}\omega_{\text{m}} \tag{2}$$

$$v_d = r_s i_d + \frac{d\lambda_d}{dt} - \omega_e\lambda_q \tag{3}$$

$$v_q = r_s i_q + \frac{d\lambda_q}{dt} + \omega_e\lambda_d \tag{4}$$

$$\omega_e = \omega_m \cdot p \tag{5}$$

In (2), the load–torque is given by $T_{\text{L}}$, the equivalent inertia of the rotor and load is given by $J_{\text{eq}}$, the friction coefficient is given by $B_{\text{eq}}$ and the mechanical rotational speed is given by $\omega_{\text{m}}$. In (3) and (4), $v_d$ and $v_q$ are the components of supply voltage vector $\boldsymbol{v}_s$, the stator resistance per phase is given by $r_s$ and the electrical rotational speed is given by $\omega_e$.

Equations (1)–(5) give a complete mathematical description of the machine, but it does not provide one with knowledge of the nonlinear behaviour of the machine. To show this, the relationship between the flux linkage vector $\boldsymbol{\lambda}_s$ and the current vector $\boldsymbol{i}_s$ has to be considered, that is FE analysis has to be used. This relationship is complex and the easiest way to describe it is by using the *dq* components, as shown in Fig. 3. Note the saturation of $\lambda_d$ with increasing $i_d$ in Fig. 3*a*, which causes the nonlinear behaviour of the PMA-RSM. At this point, the time derivatives of the flux linkages in (3) and (4) can be addresssed; these can be expanded as

$$\frac{d\lambda_d}{dt} = \frac{\partial\lambda_d}{\partial i_d}\frac{di_d}{dt} + \frac{\partial\lambda_d}{\partial i_q}\frac{di_q}{dt} + \frac{\partial\lambda_d}{\partial\theta_e}\frac{d\theta_e}{dt} \tag{6}$$

$$\frac{d\lambda_q}{dt} = \frac{\partial\lambda_q}{\partial i_d}\frac{di_d}{dt} + \frac{\partial\lambda_q}{\partial i_q}\frac{di_q}{dt} + \frac{\partial\lambda_q}{\partial\theta_e}\frac{d\theta_e}{dt} \tag{7}$$

In this paper, the effects of change of flux linkages with $\theta_e$ due to the slotted air-gap is ignored, that is the last term of (6) and the last term of (7) are taken as zero. Furthermore, in

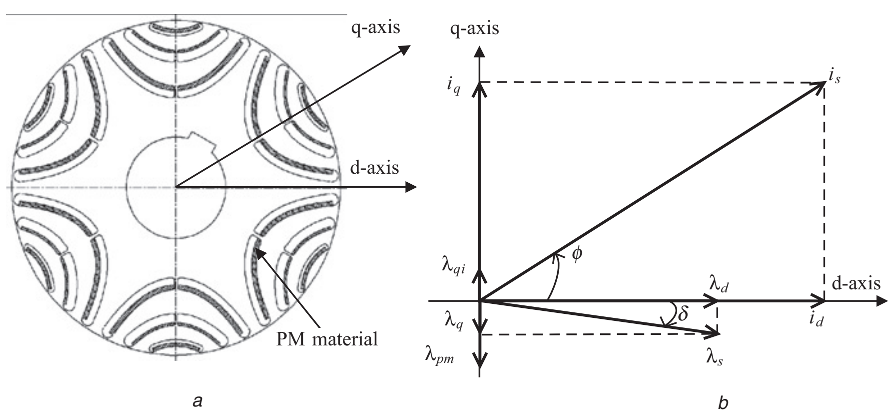


**Fig. 1** *Rotor cross-section and vector diagram*

*a* Rotor cross-section of PMA-RSM
*b* Vector diagram

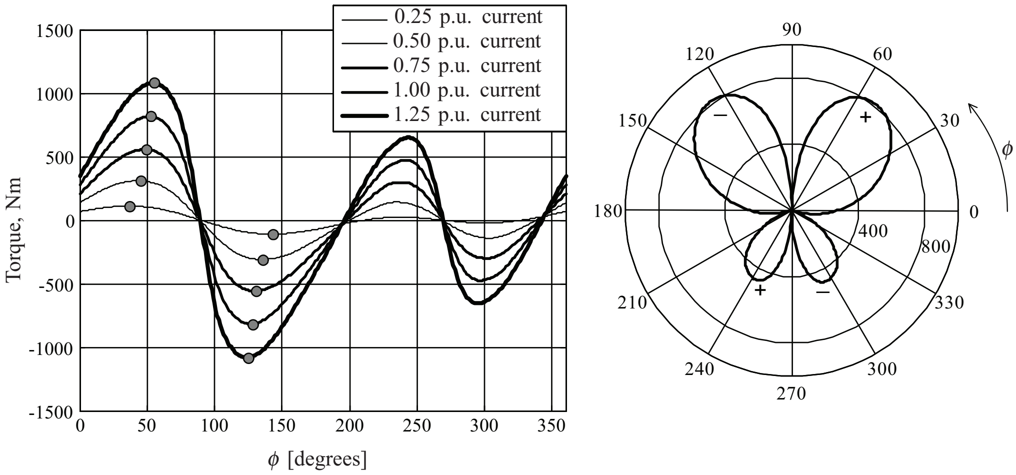


*a* *b*

**Fig. 2** *FE analysis results and polar representation*

*a* Torque as a function of $\phi$ for various current magnitudes
*b* Polar representation of absolute value of torque as a function of $\phi$ at rated current magnitude

Fig. 3, the marginal influence of $i_q$ on $\lambda_d$ and $i_d$ on $\lambda_q$ can be seen. This means that the mutual inductance for this machine is small. For further analysis, the following approximations are made

$$\frac{d\lambda_d}{dt} \simeq \frac{\partial \lambda_d}{\partial i_d}\frac{di_d}{dt} = L_d \frac{di_d}{dt} \tag{8}$$

$$\frac{d\lambda_q}{dt} \simeq \frac{\partial \lambda_q}{\partial i_q}\frac{di_q}{dt} = L_q \frac{di_q}{dt} \tag{9}$$

In the above equations, $L_d$ and $L_q$ are differential self-inductances. Performing partial derivatives on the flux linkages in Fig. 3, the graphs for $L_d$ and $L_q$ are obtained and are shown in Fig. 4. The saturation of $\lambda_d$ causes the wide range for $L_d$. In contrast, $L_q$ can be approximated as being constant.

## 3 Constant current angle control

The electrical model of the PMA-RSM in the synchronous *dq* reference frame is given by (3) and (4). The speed voltage term $\omega \cdot \lambda$ causes coupling between the equations. Furthermore, a standard linear model with constant parameters is insufficient for control system design purposes owing to the saturation of these machines during normal operation [4]. One control system design approach is a nonlinear controller that estimates the flux linkages and electrical speed using an 'adaptive back-stepping technique' [4]. The approach followed in this paper is to use data from FE analysis (in the form of LUTs) in conjunction with classical control system design. The LUTs are created using the graphs in Figs. 3 and 4 for the rated conditions.

A decoupling procedure is suggested [5, 12], whereby the speed voltage terms are calculated using flux linkages that are obtained from LUTs. The electrical speed signal is given by the observer structure, which is explained in Section 5. The calculated speed voltage terms are added or subtracted appropriately to (3) and (4) so that the equations become decoupled, as shown in (10) and (11). Note that the approximation of (8) and (9) has been used here

$$v_d' = v_d + \omega_e \lambda_q \simeq r_s i_d + L_d \frac{di_d}{dt} \tag{10}$$

$$v_q' = v_q - \omega_e \lambda_d \simeq r_s i_q + L_q \frac{di_q}{dt} \tag{11}$$

As shown in Fig. 4, $L_d$ has a large dynamic range during the normal operation of the PMA-RSM. This imposes a difficult situation for a normal PI or P current controller to be designed. This difficulty is overcome by using a LUT for $L_d$. A design criterion can be chosen so that the response time of the current loop is as fast as possible, but maintains a gain margin of $\Delta$dB at the Nyquist frequency. This criterion leads to a generic formula for a P controller and is given by (12) and (13) [5]. Note that this design method is based on the 'frequency response method', which is a classical design method [18]

$$K_d = 10^{-\Delta/20} \cdot \frac{2}{T_s} \cdot L_d \tag{12}$$

$$K_q = 10^{-\Delta/20} \cdot \frac{2}{T_s} \cdot L_q \tag{13}$$

The *d*-axis current controller gain, $K_d$, is calculated after every sampling period, $T_s$, using the latest $L_d$ that is obtained from a LUT. As shown in Fig. 4, $L_q$ can be approximated with a constant and therefore $K_q$ only has to be calculated once. The complete current controller, with the decoupling of (10) and (11), is shown in Fig. 5.

In Fig. 5, the Park and inverse Park transformations are used to convert between the stationary *abc* reference frame and the rotating *dq* reference frame. The current reference $i_s^*$, which is the output of the speed controller, can be positive or negative. The $\phi^*$ for positive torque is chosen and the absolute value of $i_q^*$ is taken to ensure operation in the upper half of the current plane, as shown in Fig. 2*b*. With the sampling period taken as $T_s = 200$ μs at the switching frequency of $f_s = 5000$ Hz and the stability

**Table 1: Machine specifications**

| | |
|---|---|
| Rated $i_s$ | 283 A |
| Rated $\phi$ | 54° or 126° |
| Rated $i_d$ | 166 A |
| Rated $i_q$ | 228 A |
| Rated torque | 812 Nm |
| Rated power | 110 kW |
| Pole pairs | 3 |
| Rated speed | 1300 rpm |

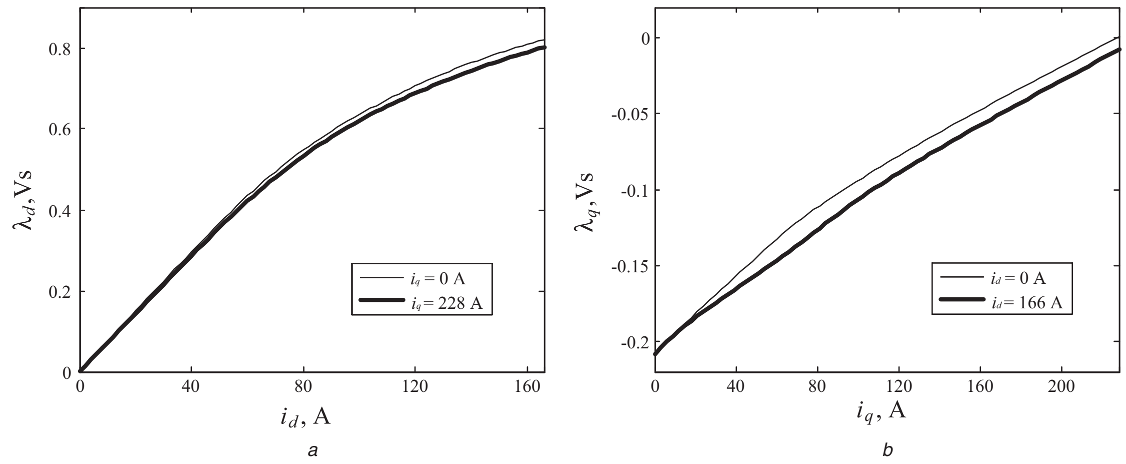


**Fig. 3** *Flux linkages*

*a* d-axis flux linkage
*b* q-axis flux linkage

margin chosen as $\Delta = 10$ dB, this current controller for the specific PMA-RSM results in a settling time of $\tau_s < 10$ ms and with no overshoot. Furthermore, in Fig. 5, the estimated rotor position is used instead of the measured rotor position; this is a step towards position sensorless control [1, 10, 11, 14]. The rotor speed is also estimated, as explained in Section 5.

## 4 Speed control

To design a PI speed controller, it is necessary to know the value of the equivalent inertia of the rotor and load, and then to choose a response time for the speed loop. In this case, the value of the inertia was found to be $J_{eq} = 2.5$ kg m$^2$. The PI speed controller, shown in Fig. 6, gives the current reference and this reference must be limited to the rated current or perhaps twice the rated current under special circumstances. This limitation on the current reference is the reason for the inclusion of integrator anti-windup in the PI controller. To simplify the design of the controller, it can be assumed that the current reaches the current reference instantly, but then the response time of the speed loop should be much longer than the response time for the current loop.

The load–torque is a disturbance input in the speed loop and will be compensated with the same response time as the speed loop. It is usually the obligation of the speed controller to compensate the load–torque. The approach followed in this paper is to assume that the load–torque will be taken care of by other means and the speed controller can be designed to be slow, relative to the current control loop. In traction applications, it is acceptable for such a large inertia machine to reach the reference speed after a few seconds. In many traction application, for example trains, the speed controller is in fact human and therefore has a response time of a few seconds. The settling time to a step input for the speed PI controller is chosen to be $\tau_s = 2$ s and the PI constants are chosen using root locus and design by emulation [18].

It is, however, not acceptable that load–torque disturbances, for example wheel-slip of locomotives, take such a long time to be compensated. The load–torque disturbance is taken care of by estimating the load–torque and calculating a compensation current reference using results from FE analysis. The speed is also estimated, because only a position signal measurement is available. The observer structure is explained in Section 5.

## 5 Load–torque and rotor speed observer

The observer structure presented here has a dual purpose: to provide a filtered speed signal for feedback to the speed PI controller and to provide an estimate of the load–torque.

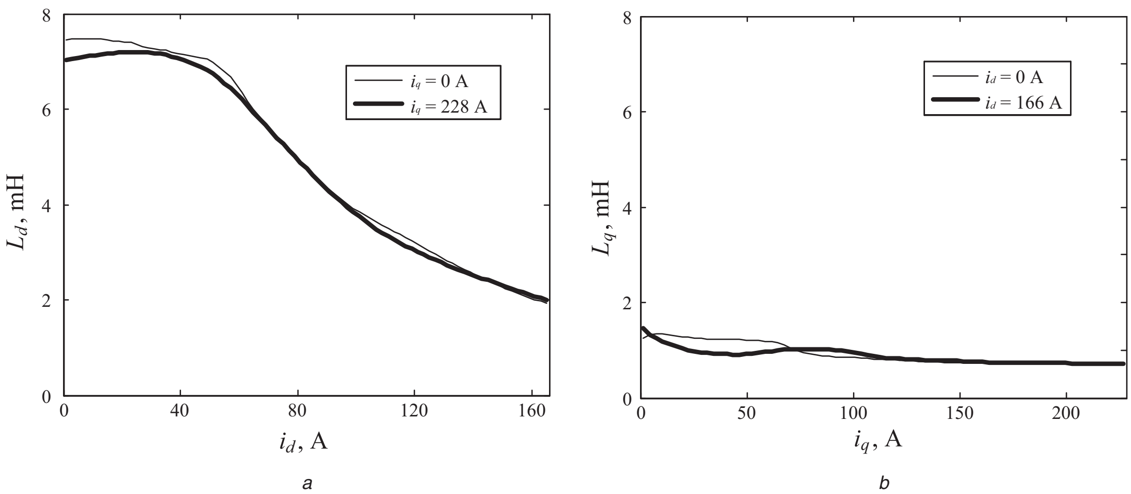


**Fig. 4** *Differential self-inductances*

*a* d-axis differential self-inductance
*b* q-axis differential self-inductance

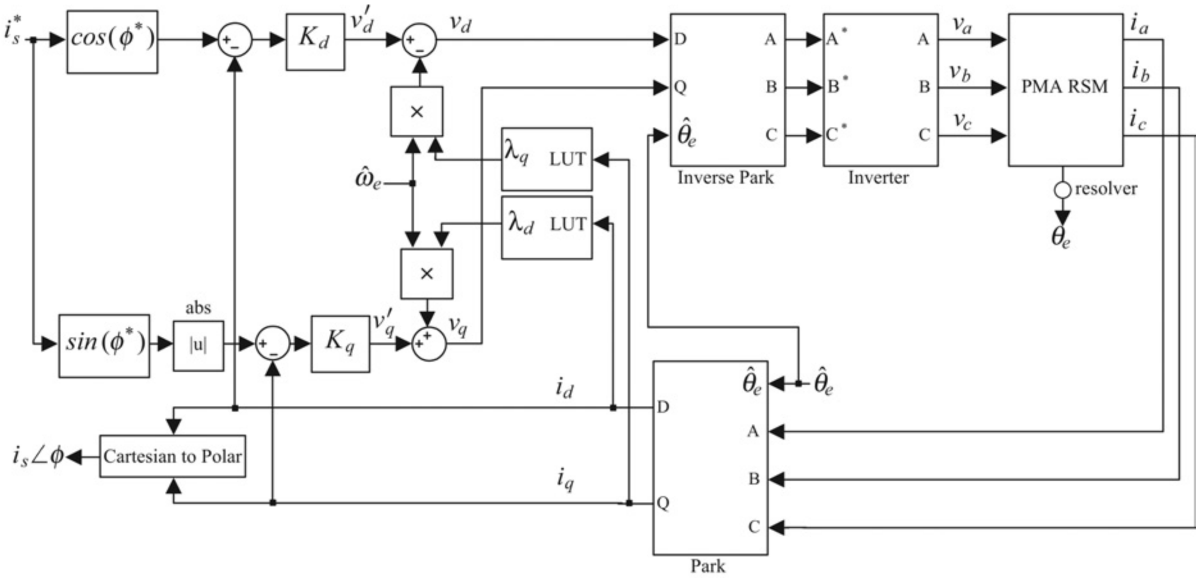


**Fig. 5** *Constant current angle control block diagram*

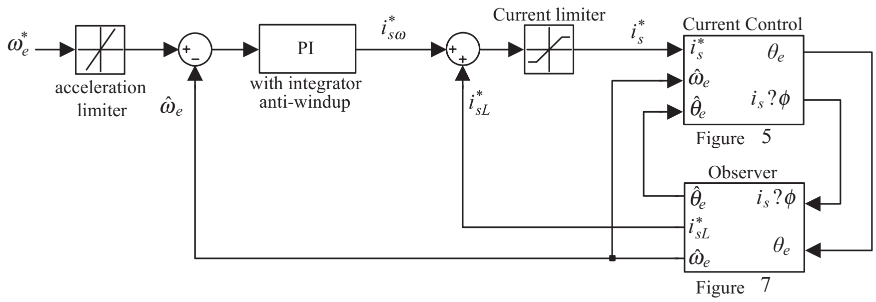


**Fig. 6** *Speed control block diagram*

A rotor position signal is obtained from a resolver. This signal can be differentiated and low-pass filtered to obtain a speed signal, but this generally results in a noisy speed signal [19]. It is possible to estimate rotor position, speed and load–torque by using the measured position signal and a model for the mechanical system of the machine.

Bearing in mind that only the position signal is measured, the plant description in the state space is

$$\begin{bmatrix} \dot{\theta}_m \\ \dot{\omega}_m \\ \dot{T}_L \end{bmatrix} = \begin{bmatrix} 0 & 1 & 0 \\ 0 & \frac{-B_{eq}}{J_{eq}} & \frac{-1}{J_{eq}} \\ 0 & 0 & 0 \end{bmatrix} \begin{bmatrix} \theta_m \\ \omega_m \\ T_L \end{bmatrix} + \begin{bmatrix} 0 \\ \frac{-1}{J_{eq}} \\ 0 \end{bmatrix} T_{em} \tag{14}$$

$$\boldsymbol{y} = \begin{bmatrix} 1 & 0 & 0 \end{bmatrix} \begin{bmatrix} \theta_m \\ \omega_m \\ T_L \end{bmatrix} \tag{15}$$

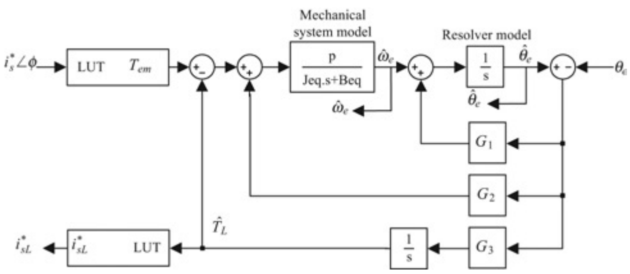


**Fig. 7** *Rotor position, speed and load–torque observer*

In this case, the value for the friction coefficient was taken to be $B_{eq} = 0.01$Nm s, although in many papers it is simply assumed to be zero. Note that the load–torque is assumed to be constant, which is generally the case in the steady state. Using a simple continuous state observer model, the observer structure is given by

$$\begin{bmatrix} \dot{\hat{\theta}}_m \\ \dot{\hat{\omega}}_m \\ \dot{\hat{T}}_L \end{bmatrix} = \begin{bmatrix} 0 & 1 & 0 \\ 0 & \frac{-B_{eq}}{J_{eq}} & \frac{-1}{J_{eq}} \\ 0 & 0 & 0 \end{bmatrix} \begin{bmatrix} \hat{\theta}_m \\ \hat{\omega}_m \\ \hat{T}_L \end{bmatrix} + \begin{bmatrix} 0 \\ \frac{-1}{J_{eq}} \\ 0 \end{bmatrix} T_{em} + \begin{bmatrix} G_1 \\ G_2 \\ G_3 \end{bmatrix} \left(\theta_m - \hat{\theta}_m\right) \tag{16}$$

Gain vector $\boldsymbol{G}$ is chosen so that the error dynamics between the real plant (PMA-RSM) and the model is relatively fast compared to the speed loop, but at the same time, the bandwidth of the estimator is limited so that the noise on the estimated speed is acceptable. The gain vector may be found using Ackerman's formula [18] for specified error dynamics pole locations. A trial-and-error procedure was used to choose the pole locations as $[-100\ -500\ -1000]$. This choise results in a settling time of 100 ms in $\hat{T}_L$ for a step input $T_L$, as shown in Fig. 11*b*, and at the same time the noise on the practical speed measurement is reasonable, as shown in Fig. 9. From (16), the block diagram for the observer is shown in Fig. 7.

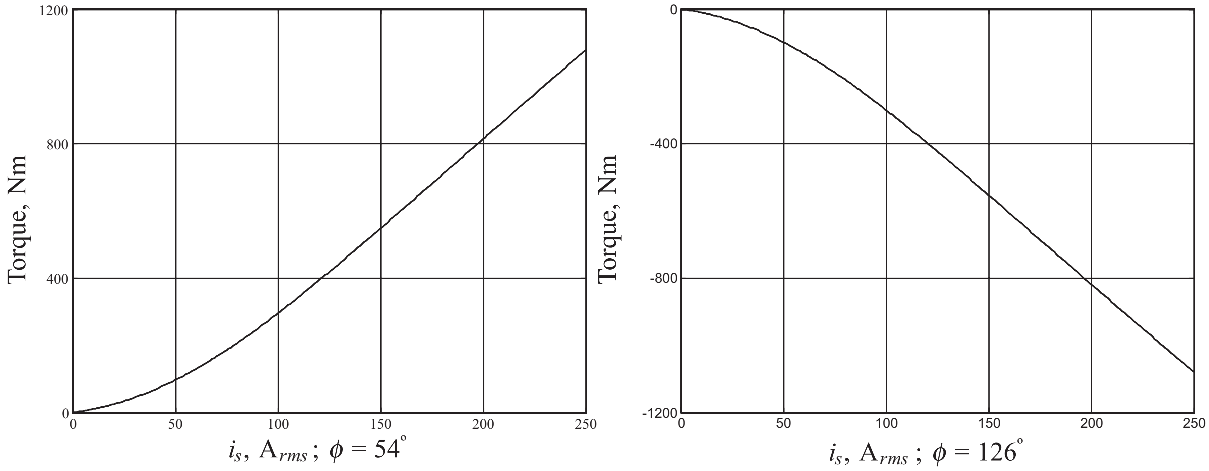


**Fig. 8** *Torque as a function of $i_s$ at rated constant $\phi$*

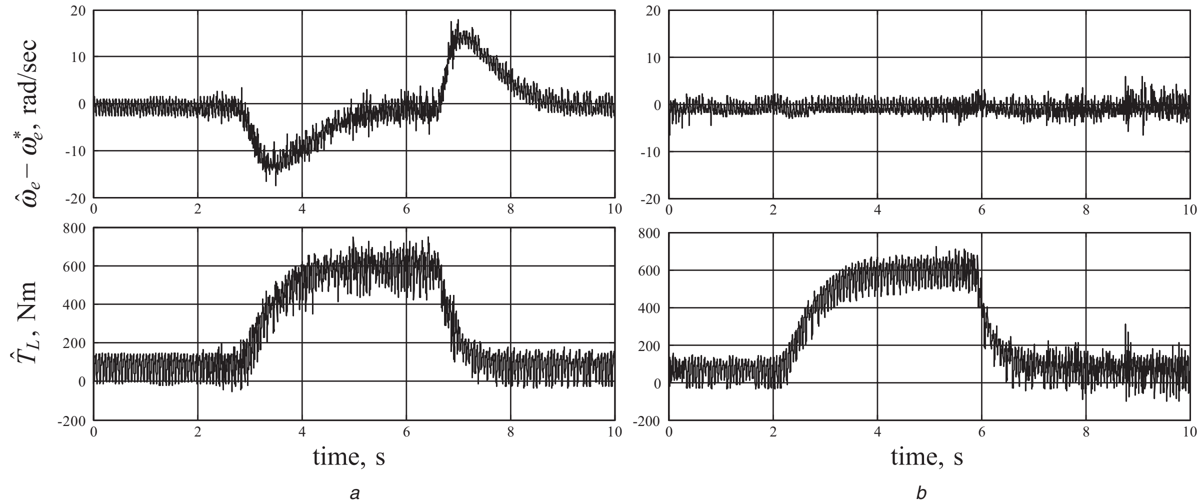


**Fig. 9** *Practical measurements*

*a* Load–torque compensation inactive
*b* Load–torque compensation active

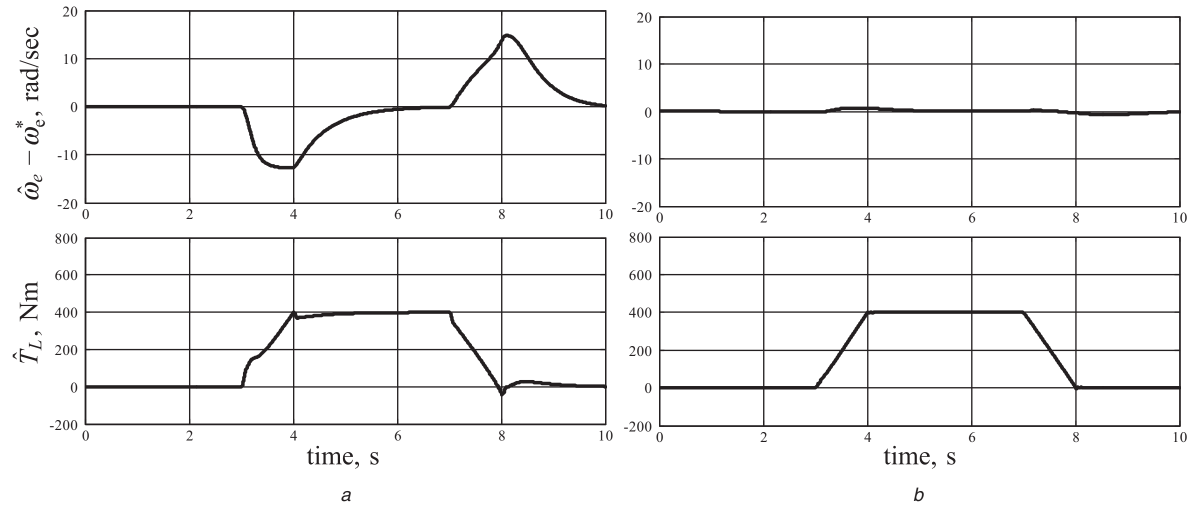


**Fig. 10** *Simulation confirmation results*

*a* Load–torque compensation inactive
*b* Load–torque compensation active

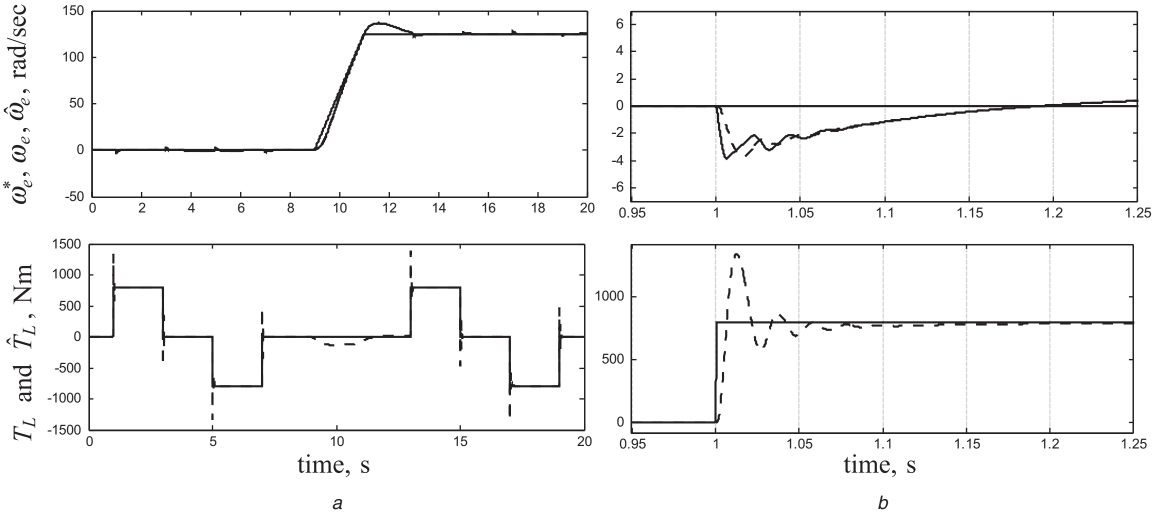


**Fig. 11** *Rated load steps at zero and rated speed simulation*

*a* Full time scale
*b* Zoomed-in time scale

Equation (14) shows that the input to the observer is $T_{em}$, but this is an unknown quantity. From Fig. 7 it is clear that $T_{em}$ is obtained using a LUT with the measured current vector as the input. This LUT is based on (1) for the rated constant $\phi^*$ as shown in Table 1, and it is neccesary because (1) is nonlinear, as shown in Fig. 8. The estimated load–torque is used as the input to another LUT (the inverse of the above-mentioned LUT) that gives the correct current reference for that load. These LUTs and accurate parameter value for $J_{eq}$ play an important role in the accuracy of the load–torque estimation. Since the observer is much more dynamic than the speed loop, the load–torque can be completely compensated for and is therefore completely decoupled from the speed loop.

## 6 Simulated and measured results

Fig. 9*a* shows results where only the PI speed controller is used. Note, however, that the PI controller was specifically designed to be used in conjunction with the load–torque observer, and its performance can be better (less overshoot, better response time), if it is not assumed that the load–torque will be taken care of by other means. The value of the overshoot is therefore not important, only the fact that there is overshoot when only the PI controller is used. Fig. 9*b* shows results where the load–torque compensation $i_{sL}$ is active. Simulated results, where the simulated load–torque is an approximation of the load–torque observed in the practical, are shown in Fig. 10. These results can be compared directly with the practical results and confirm the accuracy of the simulation. Note that the load–torque estimation is much more accurate when the compensation current is active.

With confirmed simulation accuracy, further simulation results for rated positive and negative load–torque steps at zero and rated speed are shown in Fig. 11. These results show that even with rated load–torque steps, the actual speed remains very close to the speed command. It can be noted that the estimated load–torque (shown with dotted line) is not accurate during acceleration; the effect of this on the drive performance is minimal. Due to the use of a dynamometer load-system in the practical setup, it was not possible to do a comparative practical test. These simulation results provide a good prediction of the actual drive performance.

## 7 Conclusion

It is shown that CCAC in the constant-torque speed region is a justified approximation to maximum torque per ampere control for all load conditions. If CCAC is employed, energy efficient operation of the PMA-RSM is evident, but the machine equations are nonlinear and the control system design becomes complicated. The nonlinearities, however, can easily be overcome using results from FE analysis in the form of LUTs. A classical design for proportional current controllers and a PI speed controller is augmented with a state space designed observer. Using LUTs, the observer can accurately estimate the load–torque and provide a compensation current for the load. Simulated and measured results are shown and correlate well. This research has shown that excellent dynamic performance of the PMA-RSM can be obtained using proportional current controllers, CCAC and a load–torque observer.

## 8 References


1 Guglielmi, P., Pastorelli, M., Pellegrino, G., and Vagati, A.: ‘Position-sensorless control of permanent-magnet-assisted synchronous reluctance motor’, *IEEE Trans. Ind. Appl.*, 2004, **40**, (2), pp. 615–622

2 Boldea, I., Tutelea, L., and Pitic, C.I.: ‘Pm-assisted reluctance synchronous motor/generator (pm-rsm) for mild hybrid vehicles: electromagnetic design’, *IEEE Trans Ind. Appl.*, 2004, **40**, (2), pp. 492–498

3 Vagati, A., Pastorelli, M., and Franceschini, G.: ‘High-performance control of synchronous reluctance motors’, *IEEE Trans. Ind. Appl.*, 1997, **33**, (4), pp. 983–991

4 Rahman, M.A., Vilathgamuwe, D.M., Uddin, M.N., and Tseng, K.: ‘Nonlinear control of interior permanent-magnet synchronous motor’, *IEEE Trans. Ind. Appl.*, 2003, **39**, (2), pp. 408–416

5 De Kock, H.W., and Kamper, M.J.: ‘Energy efficient current control of the permanent magnet assisted reluctance synchronous machine’. S. Afr. Univ. Power Eng. Conf. (SAUPEC), Durban, South Africa, January 2006, vol. 1, pp. 143–149

6 Xu, L., Xu, X., Lipo, T., and Novotny, D.W.: ‘Vector control of a synchronous reluctance motor including saturation and iron loss’, *IEEE Trans. Ind. Appl.*, 1991, **27**, (5), pp. 997–984

7 Betz, R.E., Lagerquist, R., Jovanovic, M., Miller, T.J.E., and Middleton, R.H.: 'Control of synchronous reluctance machines', *IEEE Trans. Ind. Appl.*, 1993, **29**, (6), pp. 1110–1121
8 Kamper, M.J., and Mackey, A.T.: 'Optimum control of the reluctance synchronous machine with a cageless flux barrier rotor', *Trans. SA Inst. Electr. Eng.*, 1995, **86**, (2), pp. 49–56
9 Matsuo, T., El-Antably, A., and Lipo, T.: 'A new control strategy for optimum-efficiency operation of a synchronous reluctance motor', *IEEE Trans. Ind. Appl.*, 1997, **33**, (5), pp. 1146–1153
10 Jovanovic, M.G., Betz, R.E., and Platt, D.: 'Sensorless vector controller for a synchronous reluctance motor', *IEEE Trans. Ind. Appl.*, 1998, **34**, (2), pp. 346–354
11 Senjyu, T., Shingaki, T., and Uezato, K.: 'Sensorless vector control of synchronous reluctance motors with disturbance torque observer', *IEEE Trans. Ind. Electron.*, 2001, **48**, (2), pp. 402–407
12 Fick, P.D., and Kamper, M.J.: 'Accurate digital current control of the reluctance synchronous machine with constant current angle', *Trans. SA Inst. Electr. Eng.*, 2004, **95**, (1), pp. 47–50
13 Lee, H., and Sul, S.: 'Efficiency-optimized direct torque control of synchronous reluctance motor using feedback linearization', *IEEE Trans. Ind. Electron.*, 1999, **46**, (1), pp. 192–198
14 Boldea, I., Janosi, L., and Blaabjerg, F.: 'A modified direct torque control (dtc) of reluctance synchronous motor sensorless drive', *Electric. Mach. Power Syst.*, 2000, **28**, (2), pp. 115–128
15 Vagati, A., Canova, A., Pastorelli, M., and Repetto, M.: 'Design refinement of synchronous reluctance motors through finite-element analysis', *IEEE Trans. Ind. Appl.*, 2000, **36**, (4), pp. 1094–1102
16 Kamper, M.J., Van der Merwe, F.S., and Willimson, S.: 'Direct finite element design optimization of the cageless reluctance synchronous machine', *IEEE Trans. Energy Convers.*, 1996, **11**, (3), pp. 547–555
17 Sibande, S.E., Kamper, M.J., and Wang, R.: 'Design and performance evaluation of a medium power pm-assisted reluctance synchronous traction machine using bonded pm-sheets', *SAIEE Afr. Res. J.*, 2006, **97**, (1), pp. 14–21
18 Franklin, G.F., Powell, J.D., and Workman, M.: 'Digital control of dynamic systems' (Addison Wesley Longman, California, 1998)
19 Lorenz, R.D., and Van Patten, K.W.: 'High-resolution velocity estimation for all-digital, ac servo drives', *IEEE Trans. Ind. Appl.*, 1991, **27**, (4), pp. 701–705